Nonequilibrium electron leakage in terahertz quantum cascade structures

Will Freeman[1,*] and Gamani Karunasiri[2]

[1]*Physics Division, Naval Air Warfare Center, China Lake, California 93555, USA*
[2]*Department of Physics, Naval Postgraduate School, Monterey, California 93943, USA*

The nonequilibrium absorption of longitudinal-optical phonons by hot electrons are studied in terahertz quantum cascade structures. We present a method for including electron leakage to the continuum that takes into account the mobility of the electrons. This is incorporated into a density matrix Monte Carlo method that includes the optical field within the resonant cavity. The effects of electron leakage to the continuum as a function of lattice temperature are discussed. Results are compared with experiment and found to be consistent. It is shown that using only confined wave functions and thereby neglecting the leakage via tunneling is inadequate for describing the electron transport.

I. INTRODUCTION

Terahertz (THz) quantum cascade (QC) laser structures[1] have been devised using several approaches[2] since their first inception,[1] and efforts to model the electron transport have allowed for the carrier dynamics to be examined on a detailed level. These types of studies have proven to be useful for solving level occupations, carrier distributions, and analyzing temperature effects. Several approaches to modeling the electron transport in QC structures have been undertaken to varying degrees of accuracy. Rate equations,[3,4] ensemble Monte Carlo method,[5–11] density matrices,[6,12–14] nonequilibrium Green's functions,[15–21] and combined approaches[22,23] have been used. Most of these studies have focused on the carrier transport, with only a few including the resonant cavity optical field in the calculations.[11,24] However, all of the THz QC structure studies have neglected the electron leakage to the continuum by using only confined wave functions in the analysis. Ignoring electron leakage is permissible only when such channels are negligible. In the THz QC laser field, there is much interest in improving the operating temperature of these devices. At elevated temperatures, the electron distributions will increase in k-space and are more prone to leaking. The quest for improving operating temperature limits will continue investigations of new structures, increasing the need for accurately modeling leakage channels in order to ensure they are minimized. For these reasons, we introduce a method for including the electron leakage in the analysis of THz QC structures and incorporate this into a density matrix Monte Carlo method.

Transport methods used for electron leakage analysis should be able to accurately estimate the current density to have confidence in the approach. This is because current density is a device characteristic that is readily measured and can sometimes be used to identify when leakage channels are present. The ensemble Monte Carlo method is a commonly used approach for modeling electron transport in QC structures, as it is one of the simplest methods to implement, but it is well known that overestimates in the current density can occur when using that approach,[22,25] particularly when scattering between weakly coupled states (states with a small anticrossing gap). The reason for this is because, in ensemble Monte Carlo simulations, generally spatially extended wave functions

are used in the calculations, and the coherence interaction is ignored. Therefore, increasing the barrier thickness between two coupled states only decreases the anticrossing gap. Thus, at resonance, the peak current density through a barrier is not affected, and only the resonance is made sharper.[25] This we know to be incorrect and inconsistent with experiment. This indicates that transport through thick barriers and between weakly coupled states is largely an incoherent process. This is also the reason why ensemble Monte Carlo simulations sometimes predict devices to work which experimentally have been found to fail.[22,25]

The density matrix Monte Carlo method[22] is one approach that can improve on these shortfalls, as it allows for dephasing[26,27] to be included in the calculations in a straightforward manner. Dephasing scattering interrupts the coherent interactions and effectively localizes the wave functions, and inclusion of dephasing is necessary to accurately describe the interaction between weakly coupled states. Because modeling the electron transport using the density matrix Monte Carlo method allows for the solution of the electron distributions for all states within a QC period, this approach is well suited for modeling the temperature dependence in QC devices. It is for these reasons that we use this method in our analysis, where we additionally incorporate a method for including the leakage due to tunneling.

II. ELECTRON TRANSPORT METHOD

In the density matrix Monte Carlo method, tight-binding wave functions localized over one QC period are used for the confined states to correctly account for dephasing, as with extended wave functions the results reduce back to the semiclassical case.[22] The intraperiod relaxation scattering is handled semiclassically as in an ensemble Monte Carlo simulation, and the transport coherence through the injector barrier is modeled using a density matrix approach that includes dephasing. The intra-QC period scattering is calculated via Fermi's golden rule, and our specific implementation of the Monte Carlo portion of this simulation and the details of the scattering rate calculations have been previously described in Ref. 28 and the transport coherence implementation described in Ref. 23.

For upper-most states that are not well confined and are more susceptible to leaking ($< \hbar \omega_{LO}$ from the barrier height), it is somewhat questionable to use localized states. For this reason, we model these states and the corresponding interactions with extended wave functions. At elevated lattice temperatures, hot electrons within these states can scatter and leak out of the confining potential to the continuum. To account for this leakage, we include a quasibound continuum-like state.[29,30] Leakage to the continuum[4] and X-valley leakage[10] have been previously modeled in mid-infrared (IR) QC structures using rate equations and an ensemble Monte Carlo approach, but here, we use the density matrix method to additionally include coherence effects.

We next discuss the scattering mechanisms included in this analysis as well as further details of the density matrix transport method. Results using this method are then compared to experimental measurements.

A. Scattering interactions

Scattering interactions including e^--LO phonon, e^--e^-, impurity, interface roughness, and photon-induced stimulated scattering rates are calculated. An effective electron temperature is used only in the screening for both the e^--e^- and impurity scattering rate calculations, where a nonequilibrium screening model[31] using a multisubband form is employed. In the rate calculations, 2D wave functions and a constant effective mass are used, and we neglect subband nonparabolicity. While both intersubband and intraband scattering rates are calculated, it is the intraband e^--LO phonon and e^--e^- scattering interactions that are the primary mechanisms responsible for thermalizing the electron gas and distributing the carriers within the subbands. It is therefore necessary to include these interactions to correctly predict the electron distributions. The electron distributions that are solved as part of this method are used in the state-blocking calculations and to calculate the density-dependent scattering rates.

The longitudinal-optical (LO) phonon scattering rates are calculated using the Fröhlich[32] interaction for bulk LO phonons, which is given by[32–35]

$$V_{e^-\text{-LO}} = \sum_{\mathbf{q}} \frac{i}{q} \sqrt{\frac{e^2 E_{LO}}{2\mathcal{V}} \left(\frac{1}{\varepsilon_\infty} - \frac{1}{\varepsilon_{st}} \right)} (a_{\mathbf{q}} - a_{-\mathbf{q}}^\dagger) e^{i\mathbf{q}\cdot\mathbf{x}}, \quad (1)$$

where $E_{LO} = \hbar \omega_{\mathbf{q}}$ is the LO phonon energy that we take as a dispersionless constant ~ 36 meV in GaAs, $\mathbf{q}$ is the LO phonon momentum vector, $\mathcal{V}$ is the quantization volume, ε_∞ and ε_{st} are the high and static frequency permittivities, and $a_{\mathbf{q}}^\dagger(a_{\mathbf{q}})$ are the creation and annihilation ladder operators. Both the e^--e^-[36,37] and ionized impurity scattering[38] rates are calculated using the Coulombic potential $V_{\text{Coul}} = \alpha/|\mathbf{x} - \mathbf{x}'|$, where $\alpha = e^2/4\pi$. The impurity scattering rates are included because the QC structures are doped. For the e^--e^- scattering,[34,39–42] antiparallel and parallel spins are taken into account by means of the exchange effect.[39,41]

Interface roughness is due to the monolayer fluctuations that are formed at the heterostructure interfaces. Scattering can occur from these imperfect growth surfaces, where the variations

in the barrier thicknesses gives way to variations in the energy levels and wave functions of the subbands. The potential for this interaction is taken to be $V_{\text{IR}} \cong \Delta(\mathbf{x}_{||}) \partial V_{\text{eff}}/\partial x_3$,[43–46] and we assume the roughness height $\Delta(\mathbf{x}_{||})$ at the in-plane position to have an exponential correlation function as given by Ref. 43. In our calculations, we use typical values of $\Delta = 1$ ML $= a/2$ and $\Lambda = 5$ nm for the roughness and correlation lengths, respectively. The photon-induced scattering rates are calculated using the electric dipole approximation $e^{-i\mathbf{q}\cdot\mathbf{x}} \sim 1$.[42,47]

B. Quantum dynamics

The density matrix method is implemented into the calculation as follows. By including only coherent transport and dephasing, the density operator equation becomes (with units of $\hbar = c = 1$)[22,23]

$$\frac{\partial \rho_{ij}}{\partial t} = \sum (-L_{ij,mn} - T'^{-1} \delta_{im} \delta_{jn}) \rho_{mn}, \quad (2)$$

where $L_{ij,mn} = H_{im} \delta_{jn} - H_{jn}^* \delta_{im}$ is the Liouville operator, which is a tetradic matrix and T' is the dephasing time used for all subbands. This equation is solved and used to describe the time evolution coherence of the electron ensemble without relaxation scattering. During the simulation, relaxation scattering is handled in the usual Monte Carlo way, but the particle ensembles are no longer integer particles as they are in the case of an ensemble Monte Carlo simulation. Scattering events where the initial state population is scattered to a final state affect the diagonal elements as $\rho_{ii,\mathbf{k}_i} \rightarrow 0$ and $\rho_{ff,\mathbf{k}_f} \rightarrow |f\rangle\langle f|$. The total dephasing time τ_{deph} is related to the relaxation scattering time τ and T' by $\tau_{\text{deph}}^{-1} = 1/2\tau^{-1} + T'^{-1}$. The factor of $1/2$ comes from the fact that $\rho_{ii} \propto |\rho_{ij}|^2$. In order to incorporate this $1/2$ factor in calculating the total dephasing time, when a scattering event occurs the off-diagonal $i \neq j$ elements are set to zero 50% of the time $\rho_{ij,\mathbf{k}_i}, \rho_{ji,\mathbf{k}_i} \rightarrow 0$ during the simulation.[22] Weighted averaging and k-space bins are used to keep from having an unbounded number of density matrices with different $\mathbf{k}_f$ values that would otherwise occur from these scattering events. A tight-binding method is used to calculate the localized basis wave functions and anticrossing gaps[23] that are used in these calculations for the confined states. Under this approximation $\mathbf{k}_{||}$ is conserved.[6]

The optical gain is calculated from density matrices, using the method outlined in Ref. 23. The contributions from all of the states are included in the calculation. Some previous density matrix analysis[48,49] has ignored any uppermost principally unused states and neglected the electron distributions. At low temperatures, these simplifications may sometimes be acceptable, as not much scattering to those states may occur, and electron distribution effects often become more pronounced at higher temperatures. However, at elevated lattice temperatures these simplifications are no longer valid due to the thermal nonequilibrium electron distributions. Using the temperature-dependent lifetimes calculated from the density matrix Monte Carlo method, the time evolution of the density operator, including the coupling between the optical

states, is solved[23]

$$\frac{\partial \rho_{ij}}{\partial t} = \sum [-i L'_{ij,mn} + W_{ji} - (W_{ji} + W_i)\delta_{ij}]\rho_{mn}, \quad i = j$$

$$= \sum \left\{ -i L'_{ij,mn} - \left[\frac{1}{2}(W_i + W_j) + T'^{-1}_{ij} \right] \delta_{im} \delta_{jn} \right\} \rho_{mn},$$

$$i \neq j, \tag{3}$$

where $L'_{ij,mn} = H'_{im}\delta_{jn} - H'^{*}_{jn}\delta_{im}$, $H'_{ij} = H_{ij} + |e|x_{ul}\mathcal{E}\cos(\omega t) \times (\delta_{iu}\delta_{jl} + \delta_{il}\delta_{ju})$, $x_{ul} = \langle l|x|u \rangle$, u and l are the upper and lower lasing state indexes respectively, W_i is the total scattering rate out of state $|i\rangle$, W_{ji} is the scattering rate from $|j\rangle \rightarrow |i\rangle$, and T'_{ij} is the pure dephasing time between states $|i\rangle$ and $|j\rangle$. Here, we treat the coupling of the optical states using the electric dipole interaction, by calculating the response to a time-harmonic electric field perturbation of the form $\mathcal{E} = \mathcal{E}\cos(\omega t)\widehat{\mathbf{x}}$. The optical states are coherently coupled through this off-diagonal term, where the optical field Rabi frequency is $\Omega_{ul} = |e|x_{ul}\mathcal{E}/\hbar$. This approach allows for the optical gain spectra to be calculated. The electrical susceptibility $\chi = \chi' + i\chi''$ can now be found from the polarization **P** induced from the optical field $\mathcal{E}$ and is $\chi(\omega) = -2|e|x_{ul}/\varepsilon\mathcal{V}_c\mathcal{E}[\rho_{ul}(\omega) + \rho_{lu}(-\omega)]$, where $\mathcal{V}_c$ is the volume of the resonant cavity. The optical gain is then calculated from

$$g(\omega) \cong \frac{k}{n_r^2}\chi''(\omega) \tag{4}$$

where k is the wave number and n_r is the refractive index. The spectra are found by solving the set of coupled first-order differential equations with time-varying coefficients of Eq. (3). In this manner, the density matrix Monte Carlo method along with Eqs. (3) and (4) allows for the temperature-dependent optical gain spectrum to be calculated. By calculating the gain spectra using density matrices, no assumption about the line shape is needed. This is useful, for instance, when calculating multiple-peaked gain spectra observed in some QC devices.[48,49]

The intensity of the optical field within the cavity is taken into account by using the classical field intensity.[11] The temporal evolution is described for each mode by

$$I(t + \Delta t) = I(t)e^{[\Gamma(\omega)g(\omega) - \alpha_m(\omega) - \alpha_w(\omega)]v\Delta t}, \tag{5}$$

where Γ is the confinement factor, $g(\omega)$ is the optical gain, α_m is the mirror loss, α_w is the waveguide loss, and v is the speed of light in the medium. During the simulation $g(\omega)$ and the optical field intensity within the cavity are updated. The photon induced stimulated scattering rates are calculated using the updated intensity from Eq. (5), as is the magnitude of optical field $\mathcal{E}$ in Eq. (3). In this manner, the saturated optical gain (which includes the optical field effects) is self-consistently calculated clamped at the threshold $g_{th} = (\alpha_m + \alpha_w)/\Gamma$.

Since leakage to the continuum is included in these calculations using a quasibound state approach,[29,30] the total current density is found as follows. It consists of carrier transport via the bound states within the wells and the carrier transport via the continuum states. The carrier transport via the bound states is calculated using the localized wave functions within the density matrix formalism. We employ classical transport analysis using the mobility of the electrons and the steady state carrier density in the continuum to estimate the
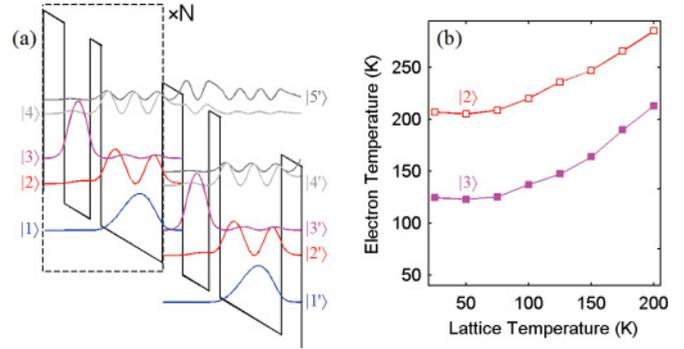
FIG. 1. (Color online) (a) Conduction band diagram of the Ref. 50 QC structure, showing the localized wave functions, extended wave function for state $|4\rangle$, and the quasibound continuum-like state $|5'\rangle$ used in this analysis. The diagonal optical transition is from $|3\rangle \rightarrow |2\rangle$ ($\Delta E_{3\text{-}2} \sim 19$ meV or 4.6 THz), and the lower lasing state is depopulated via fast intrawell e^--LO phonon scattering where $\Delta E_{2\text{-}1} \approx \hbar\omega_{\text{LO}}$. (b) The effective electron temperature of the upper and lower lasing states as a function of lattice temperature.

contribution from the continuum states. Thus, the total current density J may be written as including two components, the probability flux j from the density matrix incoherent transport and the drift current $n_{3D}^{\text{cont}}\mu_d|\mathbf{E}|$ resulting from mobility of the electrons in the continuum

$$J = |e|\left(j + n_{3D}^{\text{cont}}\mu_d|\mathbf{E}|\right), \tag{6}$$

where n_{3D}^{cont} is the population of free electrons in the continuum, μ_d is the electron drift mobility, and $|\mathbf{E}|$ is the magnitude of the applied electric field. With this approach, the effects of any leakage channels on the current density are taken into account.

III. RESULTS AND DISCUSSION

In order to validate our approach for investigating electron leakage in THz QC structures, we compare results with experimentally measured data from a $\sim$4.6 THz two-well QC structure.[50] This device uses intrawell LO phonon scattering for depopulation,[51] and measured temperature-dependent data is available. The QC structure along with the wave functions used in our calculations is shown in Fig. 1(a). In this particular structure, we model the upper most state $|4\rangle$ using an extended wave function since it is close to the barrier height and not well confined compared to the other states within the structure. At elevated lattice temperatures, hot electrons in the upper lasing state $|3\rangle$ (see Fig. 1(b) for the effective electron temperature) can scatter into state $|4\rangle$ and leak out of the confining potential to the continuum. To account for this leakage, the quasibound continuum-like state[29,30] $|5'\rangle$ is included. The $|4\rangle \leftrightarrow |5'\rangle$ interaction is modeled with these extended wave functions. The other states are more confined within the quantum well barriers and are modeled using the usual density matrix localized states. A phenomenological pure dephasing time of 0.5 psec is used in our calculations, which correspond to a dephasing scattering line width of $2\hbar/T' \approx 2.6$ meV prior to lifetime broadening. This value for the pure dephasing time is within the range of commonly accepted values,[22,48,49] which are based on measured spontaneous emission line widths.[48,52,53]
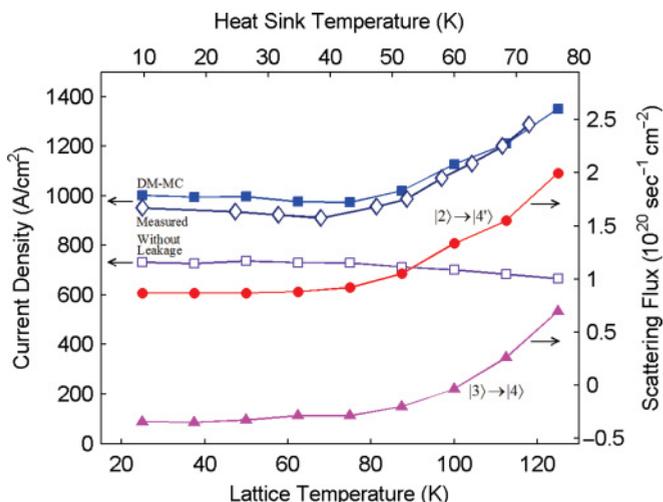
FIG. 2. (Color online) Current density as a function of lattice temperature calculated from the density matrix Monte Carlo method, with and without leakage to the continuum included. The maximum current density measured in CW mode as a function of heat sink temperature is also shown. The heat sink temperature scale is set such that, at 75 K, there is a $\Delta T = 45$ K between the lattice and heat sink temperatures. This ΔT estimate is based on the approximate difference between the pulsed and CW maximum device operating temperatures. At 10 K, a $\Delta T = 15$ K has been set corresponding to the temperature rise typically measured in QC devices. The total net scattering flux from $|3\rangle \rightarrow |4\rangle$ and that due to the incoherent transport between $|2\rangle \rightarrow |4'\rangle$ is shown, which illustrates the scattering channels into $|4\rangle$ and hence the increasing leakage at elevated lattice temperatures.

The device structure consists of 246 QC periods, yielding an overall active region thickness of ∼8 μm. It was processed into a metal-metal waveguide of 20 μm wide ($A \sim 160$ μm^2) by 1.56 mm in length.[50] Using the finite element method (FEM),[54] we calculate the facet reflectivity to be $R = 0.76$ and $\Gamma = 0.93$ at 4.6 THz. Because the applicability of the Drude model for free carrier loss in multiple quantum wells is highly questionable,[55] there is uncertainty in calculating the waveguide loss and hence the threshold using the FEM. The threshold gain measured in Ref. 56 for a similar metal-metal waveguide was reported to be $g_{th} = 36 \pm 10$ cm^{-1}. Therefore, we use the nominal measured value of $g_{th} = 36$ cm^{-1} in our calculations.

Shown in Fig. 2 is the calculated current density as a function of lattice temperature found from the density matrix Monte Carlo method, as well as the experimentally measured current density as a function of the measured heat sink temperature. A $\Delta T \sim 45$ K between the pulsed and CW maximum device operating temperatures was measured,[50] which indicates this is the approximate difference between the lattice and heat sink temperatures. Therefore, the temperature scales are set in Fig. 2 to reflect this difference at 75 K heat sink temperature, and at 10 K a $\Delta T = 15$ K has been chosen, which is the temperature rise from the cryostat cold finger we typically measure in our QC devices. It is seen in Fig. 2 that the calculated current density is in reasonably good agreement with the experimentally measured current density. The increase in current density above ∼80 K is correctly

predicted when the electron leakage and the electron mobility are included in the calculations, as done in these density matrix Monte Carlo simulations where a temperature-independent electron mobility of 8,500 cm^2 V^{-1} sec^{-1} has been used. Also shown is the current density solved without including leakage (with only confined wave functions used in the analysis) as has been done in all previous THz QC device studies. It is seen that, without leakage taken into account, the sharp rise in current density with increasing lattice temperature is not correctly calculated. It is the electron mobility drift current portion of the computation that is largely responsible for correctly calculating this increase in current density. This analysis not only quantitatively confirms the presence of hot nonequilibrium electron leakage in this structure (something previously qualitatively speculated[50]), but additionally reveals a previously unidentified $|2\rangle \rightarrow |4'\rangle$ leakage channel to be dominant. This can be seen from the computed total scattering flux due to the net scattering between $|3\rangle \rightarrow |4\rangle$ and the incoherent transport between $|2\rangle \rightarrow |4'\rangle$, as shown in Fig. 2. It is seen that the $|2\rangle \rightarrow |4'\rangle$ channel dominates the filling of state $|4\rangle$, and hence the continuum leakage via $|4\rangle \rightarrow |5'\rangle$ as well as that from electrons with sufficient in-plane kinetic energy that are unbound from the potential barrier $E_n + E_{k_\parallel} > V_b$. This is particularly evident at the lower cryogenic temperatures where the scattering flux from $|3\rangle \rightarrow |4\rangle$ is negative, indicating more back-scatter than forward scattering. The $|3\rangle \rightarrow |4\rangle$ scattering, which directly affects the population inversion, becomes more pronounced above ∼85 K when the LO phonon absorption process becomes noticeably thermally active. Nevertheless, the $|2\rangle \rightarrow |4'\rangle$ incoherent transport continues to dominate and is over two times greater at 125 K. Without inclusion of scattering to the quasibound state $|5'\rangle$ and taking into account the drift current as well as the nonequilibrium electron distributions, this increase in current density is not correctly accounted. Because of the $|2\rangle \rightarrow |4'\rangle$ transport, when leakage to the continuum is neglected in the calculations, the current density is underestimated even at 25 K (see Fig. 2). Thus, density matrix calculations which only include confined tight-binding wave functions will not produce results consistent with experiment in structures where appreciable leakage to the continuum takes place, particularly at elevated lattice temperatures.

The peak optical power is obtained from the mode intensity inside the cavity as $P = 1/2\, I A (1 - R)/\Gamma$, and computed to be about 2 mW at a lattice temperature of 25 K and at the reported peak emission frequency of 4.7 THz. The uncorrected optical power reported in Ref. 50 is ∼0.5 mW measured at a heat sink temperature of 10 K. The optical power value we compute corresponds to a collection efficiency of ∼25%, which is close to the collection efficiency others have estimated.[57] Now if the threshold gain is less than the 36 cm^{-1} value we used in our calculations, to be consistent with experiment and predict the same measured peak optical power would also require the collection efficiency to be less. The computed current density would then also increase slightly at 25 K, even without leakage taken into account. This would possibly indicate the contribution computed from the $|2\rangle \rightarrow |4'\rangle$ leakage channel could be slightly high. However, we were not able to predict the sharp increase in the current density with increasing lattice temperature without including
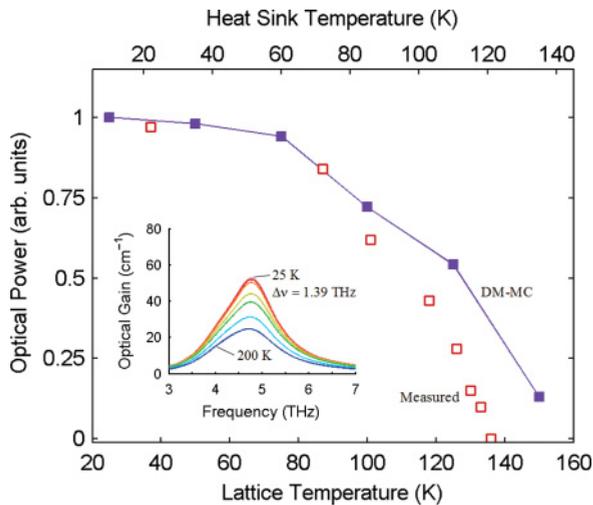
FIG. 3. (Color online) Peak optical gain as a function of lattice temperature calculated from the density matrix Monte Carlo method and the peak device optical power measured in pulsed mode. A $\Delta T = 15$ K between the lattice and heat sink temperature scales is set. Shown in the inset is the corresponding calculated unsaturated temperature-dependent optical gain spectra.

the leakage to the continuum and the electron mobility drift current.

The computed optical power as a function of lattice temperature, normalized to correct for the collection efficiency, is shown in Fig. 3. The measured device optical power as a function of heat sink temperature is also included. A $\Delta T = 15$ K between the lattice and heat sink temperature scales is chosen for this pulsed case. We find reasonable agreement with the calculated optical power as a function of temperature compared to that of the measured peak optical power curve. The optical power is predicted to be slightly higher around ~ 135 K. One explanation for this could be the difference between the lattice and measured heat sink temperatures at elevated lattice temperatures is likely higher than the

15 K value assumed in Fig. 3. Although the spontaneous emission spectra were not reported as being measured for this device, included inset in Fig. 3 is the calculated unsaturated temperature-dependent optical gain spectra, where a line width of $\Delta \nu = 1.39$ THz at 25 K is computed for this structure.

It should be noted that, while extended states were used for the leakage analysis, localized states could also be used, provided the quasibound state is localized over one QC period. When this was done in our calculations, the results were nearly the same. This is as expected due to the large ~ 10 meV anticrossing gap computed for the leakage coupling.

The results from using this method for including the temperature-dependent electron leakage to the continuum, incorporated into a density matrix Monte Carlo simulation, were found to be consistent with experiment. This approach is applicable for any QC structure, especially when the nonequilibrium electron distributions may be leaking to the continuum. This method is useful for identifying potential leakage channels, particularly in new structures intended to operate at elevated lattice temperatures. The limiting mechanisms identified suggest not only leakage from the upper lasing state should be minimized, but leakage from other states that may not be intended to be used should also be minimized. These types of thermally active leakage channels may not be easy to identify without performing this type of analysis, especially in new structures under study. Using density matrices to calculate the temperature-dependent optical gain spectra may also be useful for analyzing devices that may not have simple Lorentzian temperature-dependent shaped gain spectra. Our analysis shows the importance of including leakage and the electron mobility, as well as incoherent transport, in the calculations of THz QC structures. It also shows that including only confined wave functions in the analysis is inadequate for describing electron transport leakage.

*Corresponding author: will.freeman@navy.mil

[1] R. Köhler, A. Tredicucci, F. Beltram, H. E. Beere, E. H. Linfield, A. G. Davies, D. A. Ritchie, R. C. Iotti, and F. Rossi, Nature (London) **417**, 156 (2002).

[2] B. S. Williams, Nature **1**, 517 (2007).

[3] P. Harrison, Appl. Phys. Lett. **75**, 2800 (1999).

[4] D. Indjin, P. Harrison, R. W. Kelsall, and Z. Ikonić, Appl. Phys. Lett. **81**, 400 (2002).

[5] C. Jacoboni and L. Reggiani, Rev. Mod. Phys. **55**, 645 (1983).

[6] R. C. Iotti and F. Rossi, Phys. Rev. Lett. **87**, 146603 (2001).

[7] R. Köhler, R. C. Iotti, A. Tredicucci, and F. Rossi, Appl. Phys. Lett. **79**, 3920 (2001).

[8] H. Callebaut, S. Kumar, B. S. Williams, Q. Hu, and J. L. Reno, Appl. Phys. Lett. **83**, 207 (2003).

[9] O. Bonno, J.-L. Thobel, and F. Dessenne, J. Appl. Phys. **97**, 043702 (2005).

[10] X. Gao, D. Botez, and I. Knezevic, Appl. Phys. Lett. **89**, 191119 (2006).

[11] C. Jirauschek, Appl. Phys. Lett. **96**, 011103 (2010).

[12] I. Waldmüller, W. W. Chow, E. W. Young, and M. C. Wanke, IEEE J. Quantum Electron. **42**, 292 (2006).

[13] I. Savic, N. Vukmirovic, Z. Ikonić, D. Indjin, R. W. Kelsall, P. Harrison, and V. Milanovic, Phys. Rev. B **76**, 165310 (2007).

[14] C. Weber, F. Banit, S. Butscher, A. Knorr, and A. Wacker, Appl. Phys. Lett. **89**, 091112 (2006).

[15] S.-C. Lee and A. Wacker, Phys. Rev. B **66**, 245314 (2002).

[16] F. Banit, S.-C. Lee, A. Knorr, and A. Wacker, Appl. Phys. Lett. **86**, 041108 (2005).

¹⁷S.-C. Lee, F. Banit, M. Woerner, and A. Wacker, Phys. Rev. B **73**, 245320 (2006).

¹⁸R. Nelander and A. Wacker, Appl. Phys. Lett. **92**, 081102 (2008).

¹⁹T. Kubis, C. Yeh, and P. Vogl, Phys. Status Solidi C **5**, 232 (2008).

²⁰T. Kubis, C. Yeh, P. Yogl, A. Benz, G. Fasching, and C. Deutsch, Phys. Rev. B **79**, 195323 (2009).

²¹T. Schmielau and M. F. Pereira, Phys. Status Solidi B **246**, 329 (2009).

²²H. Callebaut and Q. Hu, J. Appl. Phys. **98**, 104505 (2005).

²³W. Freeman and G. Karunasiri, Proc. SPIE **8119**, 81190A (2011).

²⁴R. C. Iotti and F. Rossi, Rep. Prog. Phys. **68**, 2533 (2005).

²⁵Q. Hu, B. S. Williams, S. Kumar, H. Callebaut, S. Kohen, and J. L. Reno, Semicond. Sci. Technol. **20**, 228 (2005).

²⁶R. F. Kazarinov and R. A. Suris, Sov. Phys. Semicond. **5**, 707 (1971).

²⁷C. Sirtori, F. Capasso, J. Faist, A. L. Hutchinson, D. L. Sivco, and A. Y. Cho, IEEE J. Quantum Electron. **34**, 1722 (1998).

²⁸W. Freeman and G. Karunasiri, Proc. SPIE **7311**, 7311V (2009).

²⁹R. Q. Yang and J. M. Xu, Phys. Rev. B **46**, 6969 (1992).

³⁰C. Sirtori, F. Capasso, and J. Faist, Phys. Rev. B **50**, 8663 (1994).

³¹T. Ando, A. B. Fowler, and F. Stern, Rev. Mod. Phys. **54**, 437 (1982).

³²H. Fröhlich, Proc. Roy. Soc. A **160**, 230 (1937).

³³J. P. Leburton, J. Appl. Phys. **56**, 2850 (1984).

³⁴S. Goodnich and P. Lugli, Phys. Rev. B **37**, 2578 (1988).

³⁵H. B. Teng, J. P. Sun, and G. I. Haddad, J. Appl. Phys. **84**, 2155 (1998).

³⁶I. Waldmüller, J. Förstner, S.-C. Lee, A. Knorr, M. Woerner, K. Reimann, R. A. Kaindl, T. Elsaesser, R. Hey, and K. H. Plogg, Phys. Rev. B **69**, 205307 (2004).

³⁷T. Shih, K. Reimann, M. Woerner, T. Elsaesser, I. Waldmüller, A. Knorr, R. Hey, and K. H. Plogg, Phys. Rev. B **72**, 195338 (2005).

³⁸H. Callebaut, S. Kumar, B. S. Williams, Q. Hu, and J. L. Reno, Appl. Phys. Lett. **84**, 645 (2004).

³⁹M. Moško, A. Mošková, and V. Cambel, Phys. Rev. B **51**, 16860 (1995).

⁴⁰A. Tomita, J. Shah, J. E. Cunningham, S. M. Goodnick, P. Lugli, and S. Chuang, Erratum: Phys. Rev. B **52**, 5445 (1995).

⁴¹P. Kinsler, P. Harrison, and R. W. Kelsall, Phys. Rev. B **58**, 4771 (1998).

⁴²W. Freeman, Ph.D. Dissertation, Naval Postgraduate School, Department of Physics (2009) [http://edocs.nps.edu/npspubs/scholarly/].

⁴³S. M. Goodnick, D. K. Ferry, C. W. Wilmen, Z. Liliental, D. Fathy, and O. L. Krivanek, Phys. Rev. B **32**, 8171 (1985).

⁴⁴B. K. Ridley, in *Theory of Transport Properties of Semiconductor Nanostructures*, edited by E. Scholl (Chapman & Hall, London, 1998), p. 357.

⁴⁵T. Unuma, M. Yoshita, T. Noda, H. Sakaki, and H. Akiyama, J. Appl. Phys. **93**, 1586 (2003).

⁴⁶D. K. Ferry and S. M. Goodnick, *Transport in Nanostructures* (Cambridge University Press, Cambridge, 2008).

⁴⁷B. K. Ridley, *Quantum Processes in Semiconductors* (Oxford University Press, Oxford, 1999).

⁴⁸S. Kumar and Q. Hu, Phys. Rev. B **80**, 245316 (2009).

⁴⁹E. Dupont, S. Fathololoumi, and H. C. Liu, Phys. Rev. B **81**, 205311 (2010).

⁵⁰S. Kumar, C. W. I. Chan, Q. Hu, and J. L. Reno, Appl. Phys. Lett. **95**, 141110 (2009).

⁵¹W. Freeman and G. Karunasiri, Proc. Ninth Int. Conf. on Intersubband Transitions in Quantum Wells (2007) [http://www.itqw07.leeds.ac.uk/].

⁵²G. Scalari, L. Ajili, J. Faist, H. Beere, E. Linfield, D. Ritchie, and G. Davies, Appl. Phys. Lett. **82**, 3165 (2003).

⁵³J. Kröll, J. Darmo, S. S. Dhillon, X. Marcadet, M. Calligaro, C. Sirtori, and K. Unterrainer, Nature **449**, 698 (2007).

⁵⁴COMSOL Multiphysics and ANSYS HFSS were used for the FEM modeling.

⁵⁵B. S. Williams, S. Kumar, and Q. Hu, Opt. Express **13**, 3331 (2005).

⁵⁶L. A. Dunbar, R. Houdré, G. Scalari, L. Sirigu, M. Giovannini, and J. Faist, Appl. Phys. Lett. **90**, 141114 (2007).

⁵⁷A. Tredicucci, R. Köhler, L. Mahler, H. E. Beere, E. H. Linfield, and D. A. Ritchie, Semicond. Sci. Technol. **20**, S222 (2005).